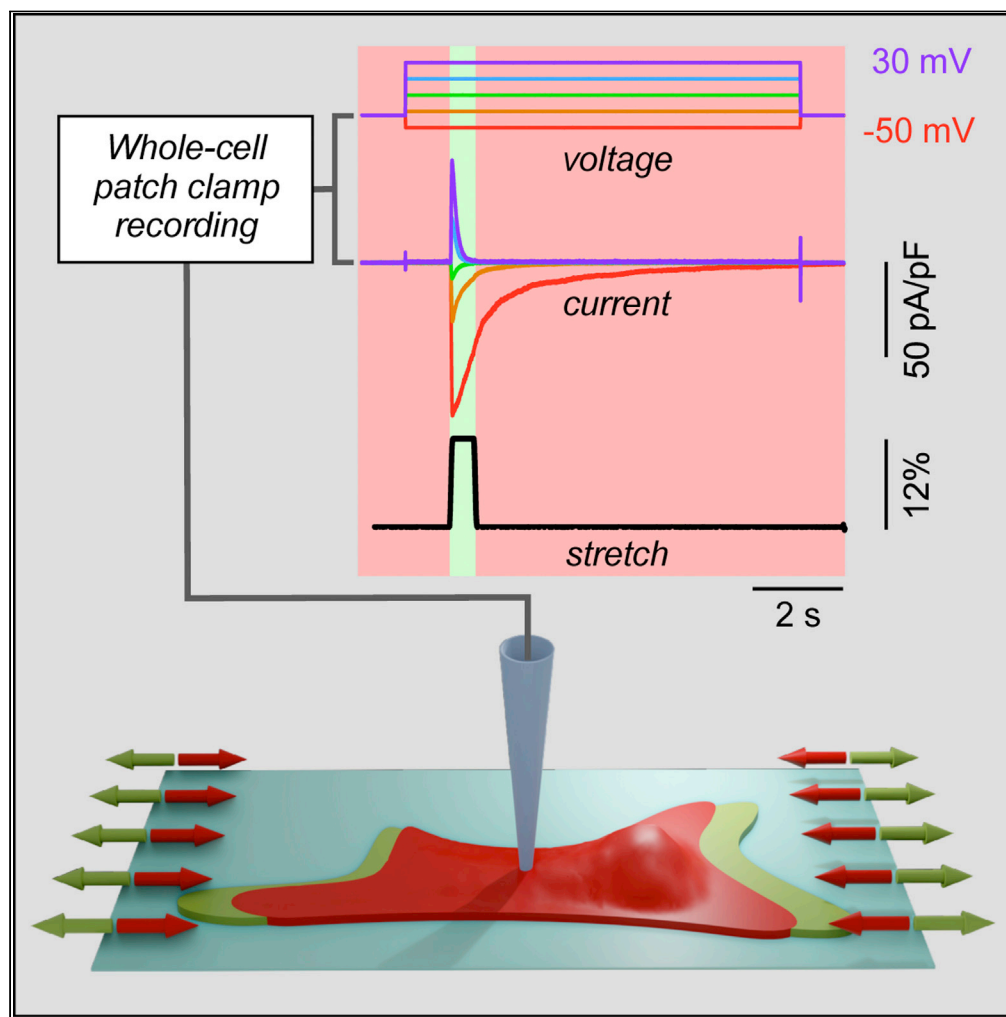


Article

Advancing mechanobiology by performing whole-cell patch clamp recording on mechanosensitive cells subjected simultaneously to dynamic stretch events



Etienne de Coulon, Christian Dellenbach, Stephan Rohr

etienne.decoulon@unibe.ch (E.d.C.)
stephan.rohr@unibe.ch (S.R.)

HIGHLIGHTS

The methodology presented enables investigations of adherent mechanosensitive cells

Whole-cell patch-clamp recording is performed while cells are dynamically stretched

Continuous recording of sequences of physiological mechanical stimuli is practicable

Experiments with NIH3T3 cells reveal a robust atypical mechanosensitive current

de Coulon et al., iScience 24, 102041
February 19, 2021 © 2021 The Author(s).
<https://doi.org/10.1016/j.isci.2021.102041>

Article

Advancing mechanobiology by performing whole-cell patch clamp recording on mechanosensitive cells subjected simultaneously to dynamic stretch events

Etienne de Coulon,^{1,*} Christian Dellenbach,¹ and Stephan Rohr^{1,2,*}

SUMMARY

A comprehensive understanding of mechano-electrical coupling requires continuous intracellular electrical recordings being performed on cells undergoing simultaneously *in vivo* like strain events. Here, we introduce a linear strain single-cell electrophysiology (LSSE) system that meets these requirements by delivering highly reproducible unidirectional strain events with magnitudes up to 12% and strain rates exceeding $200\%s^{-1}$ to adherent cells kept simultaneously in whole-cell patch-clamp recording configuration. Proof-of-concept measurements with NIH3T3 cells demonstrate that stable recording conditions are maintained over tens of strain cycles at maximal amplitudes and strain rates thereby permitting a full electrophysiological characterization of mechanically activated ion currents. Because mechano-electrical responses to predefined strain patterns can be investigated using any adherent wild-type or genetically modified cell type of interest, the LSSE system offers the perspective of providing advanced insights into mechanosensitive ion channel function that can finally be compared quantitatively among different types of channels and cells.

INTRODUCTION

Mechanical cues are ubiquitous in biology and importantly determine body function in health and disease (Gordon et al., 2020; Janmey et al., 2020; Quinn and Kohl, 2021). The transduction of mechanical events into physiological or pathological signals commonly depends on the activation of mechanosensitive ion channels (Ranade et al., 2015) that induce mechanically activated (MA) currents thereby converting mechanical events into electrical signals (mechano-electrical coupling, Quinn et al., 2014). Standard methods used to investigate mechanosensitive ion channels are based on performing whole-cell patch-clamp experiments on cells that are mechanically stimulated by osmotic interventions (Numata et al., 2007), shear stress (Carreon et al., 2017; Olesen et al., 1988), subcellular nanopillar movements (Poole et al., 2014), or cell membrane indentation using a second pipette (Hao and Delmas, 2011; McCarter et al., 1999), which represents the most widely used approach. In cell-attached recording configuration, mechanosensitive ion channels have been analyzed using high-speed pressure clamp systems (Besch et al., 2002; Guharay and Sachs, 1984). With the exception of, e.g., shear stress acting on adherent endothelial cells, osmotic stress acting on osmoreceptors, or subcellular focal movements exerted by single nanopillars, existing methodologies for straining cells have little in common with *in vivo*-like strain patterns (Sachs, 2018), which consist predominantly of uniaxial strains acting on entire cells. Moreover, MA currents elicited by local membrane indentation or high-speed pressure clamp systems cannot be extrapolated to whole-cell currents or to the situation *in vivo* in quantitative terms (Sachs, 2015). To overcome these shortcomings, we developed a linear strain single-cell electrophysiology (LSSE) system that permits subjecting adherent cells kept in whole-cell patch-clamp recording configuration to predefined uniaxial strain events that reproduce the magnitude, dynamics, and directional alignment of strains occurring *in vivo*. Taking heart mechanics as a benchmark, it was the goal to develop a strain system that offers strain amplitudes in excess of 9% and strain kinetics surpassing $38\%s^{-1}$ as reported before for pig hearts (Ferraioli et al., 2019). Ideally, the system should also replicate the mechanics of mice hearts where amplitudes are similar (10%) but strain kinetics ($320\%s^{-1}$) are substantially higher (Kobirumaki-Shimozawa et al., 2016). Proof-of-concept measurements demonstrate that fibroblastic NIH3T3 cells, after being stretched beyond a distinct threshold, develop substantial MA currents that exhibit voltage-dependent inactivation kinetics and show slow recovery from inactivation.

¹Department of Physiology, University of Bern, Bülhlplatz 5, Bern, CH-3012, Switzerland

²Lead contact

*Correspondence: etienne.decoulon@unibe.ch (E.d.C.), stephan.rohr@unibe.ch (S.R.)
<https://doi.org/10.1016/j.isci.2021.102041>



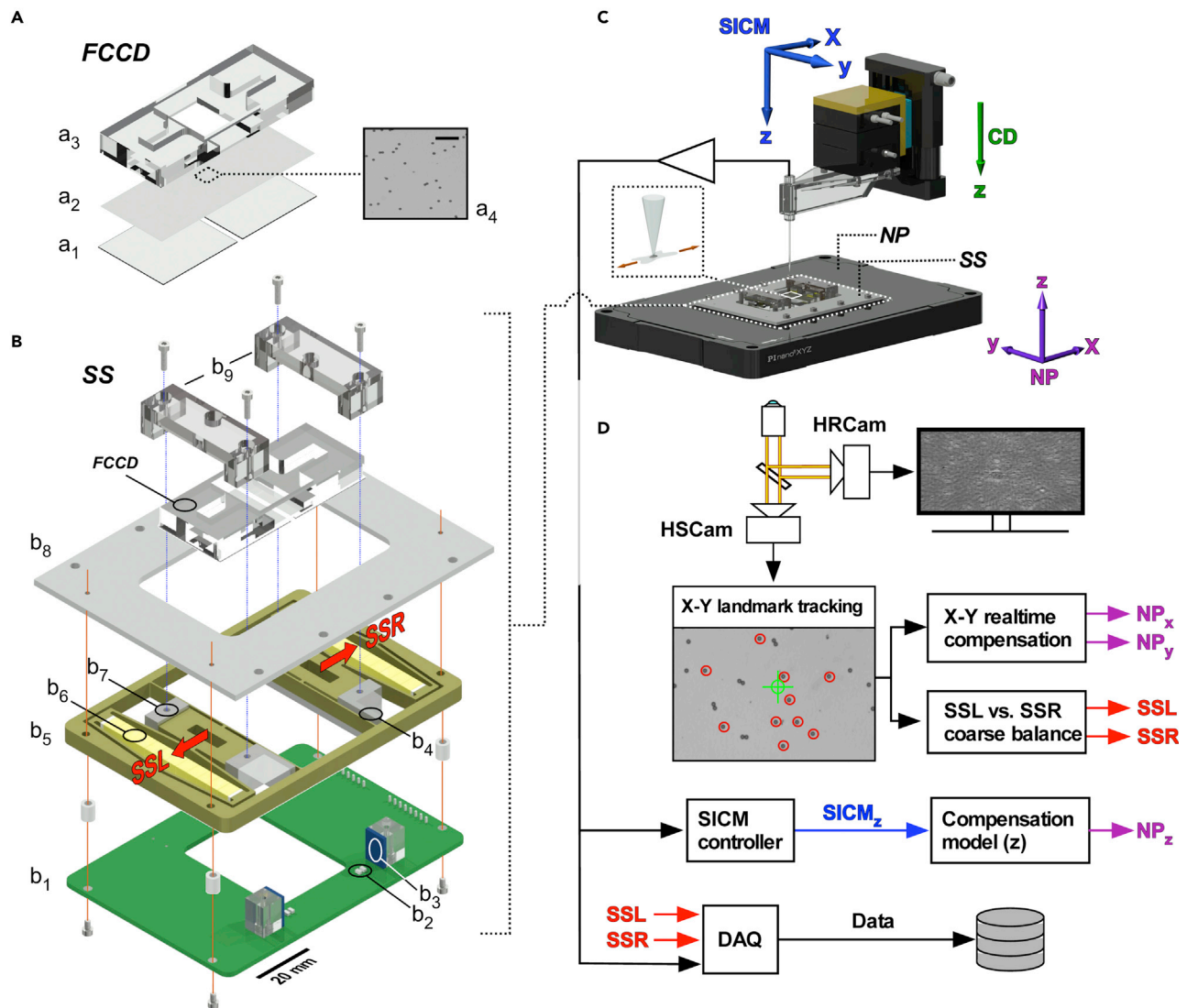


Figure 1. Components of the linear strain single-cell electrophysiology (LSSE) system

(A) Flexible cell culture dish (FCCD): (a1) glass support, (a2) compliant silicone membrane, (a3) compliant polydimethylsiloxan culture well. The micrograph (a4) depicts the landmarks formed by black-dyed polystyrene beads in the region of the FCCD undergoing strain (scale bar, 50 μ m).

(B) Strain stage (SS): (b1) printed circuit board (PCB) with inductive stage displacement sensing consisting of (b2) resonance circuit capacitors, (b3) resonance circuit planar inductors, and (b4) conductive winglets; (b5) compliant titanium strain stage with (b6) piezostack actuator and (b7) mounting threads for the FCCD brackets: strain stage left (SSL) refers to left-directed strain and SSR to right-directed strain; (b8) SS assembly and cover plate; (b9) mounting clamps for the FCCD.

(C) Overview of the electromechanical components of the LSSE system consisting of the SS that is fixed to a 3-axis nanopositioner (NP). The patch pipette is mounted on a 3-axis scanning ion conductance microscope (SICM) that is attached to a single axis coarse z drive (CD).

(D) Block diagram of the control and data acquisition subsystems. Images of the cells under investigation are acquired by a high-resolution camera (HRCam) connected to an inverted microscope. Data from x-y landmark tracking with a high-speed camera (HSCam) are used for SSR versus SSL coarse balancing and real-time x-y displacement compensation by NP_x and NP_y during strain application. The z-channel signal of the SICM is exploited for generating a model predicting z axis compensation via NP_z during the actual experiment (feedforward control).

RESULTS

Components of the linear strain single-cell electrophysiology system

The system presented permits applying physiological levels of uniaxial strain to single adherent cells while simultaneously performing patch-clamp recordings. In essence, this is achieved by combining a strain stage delivering the required dynamics with an ultraprecise spatial stabilization system that maintains the delicate gigaseal formed by the patch pipette on the cell surface intact during strain-induced cell movements. An overview of the system

components that fulfill these requirements is shown in Figure 1. Central to the LSSE system is a flexible cell culture dish (FCCD; Figure 1A) that is composed of a pre-stretched 50- μm thin silicone membrane that is plasma bonded to two glass supports being separated by 2 mm. Compliant culture wells cast in polydimethylsiloxane (PDMS) are bonded to the pre-stretched silicone membrane with PDMS, and the underside of the FCCD is sprayed with black-dyed polystyrene beads (6 μm diameter) that serve as optical landmarks enabling stabilization of the cell micropipette-electrode interface during strain application. For experiments, FCCDs containing single cultured cells are fixed by a pair of brackets to the piezo-actuated strain stage (SS; Figure 1B). The core of this stage consists of a compliant structure made of electric-discharge machined titanium that is driven by piezostack actuators. The kinematic structure of the compliant mechanism is formed by two opposing diamond frames that amplify and redirect the stroke of the piezostacks along two antiparallel axes (for finite element analysis cf. Figure S1). Each diamond frame is connected to an FCCD mounting interface that is anchored to a leaf spring to increase out-of-plane stiffness. For closed-loop positioning control, the relative position of each FCCD mounting interface is measured by contactless inductive sensors installed on a printed circuit board (PCB) board. The sensors are composed of resonant circuits whose frequencies are modulated by the distance between the planar inductors and the conductive winglets that protrude laterally from each FCCD mounting interface. Stack-mounting of the PCB, the titanium structure, and the cover plate completes the strain stage. During experiments, the strain stage is mechanically fixed to a 3D positioning control system (Figure 1C) consisting of a 3-axis nanopositioner (NP; Figure 1C) that stabilizes the cell-micropipette interface in all principal directions while the patched cells are strained. The system is completed by a scanning ion conductance microscope (SICM; 3-axis NP cube) to which the patch pipette is fixed by means of a cantilever. Fast approach of the pipette to the cell is supported by a coarse linear drive (CD; Figure 1C) that moves the SICM cube in z-direction. The entire LSSE system is mounted on the stage of an inverted microscope equipped for epifluorescence.

A block diagram of the spatial stabilization control system that sustains the pipette-cell interface during strain application is shown in Figure 1D. The task is divided into in-plane (x-y) and out-of-plane (z) stabilization. In-plane compensation is addressed by a two-step strategy: (1) Before establishing the gigaseal, a coarse compensation of strain-induced movement of the target cell along the principal strain axis is performed by balancing left-directed actuation of the strain stage (SSL, Figure 1D) versus right-directed actuation of the strain stage (SSR, Figure 1D) such that the target cell shows minimal x axis displacement during strain application (Figure S2). (2) Residual in-plane displacements are compensated in real-time during the experiments by tracking the optical landmarks during strain pulses using a high-speed camera (HScam, Figure 1D) operating at 200 Hz. From the actual position of the landmarks, the relative x-y displacements between the cell and the patch pipette are calculated and the respective compensation signals sent to the NP (closed-loop control; NP_x , NP_y ; Figures 1D and S3). Out-of-plane (z) displacement during strain is compensated by a feedforward method: before the actual experiment, the system response in z-direction is assessed by the SICM. Based on this response, the compensation (NP_z Figure 1D) is computed and subsequently controls the NP during each strain event (Figure S4).

Maximal strain rates and amplitudes provided by the LSSE system

The characteristics of in-plane strains developed by the LSSE system were assessed by tracking x-y displacements of the landmarks during application of trapezoidal strains exhibiting defined amplitudes and dynamics. As shown in Figure 2A, the piezo-actuated stage produced strains along the principal direction (ϵ_x) of up to 12%. Strains measured simultaneously in perpendicular direction (ϵ_y) indicated the presence of a small amount of compressive transversal strain. The results of identical measurements in six additional FCCDs shown in Figure 2B demonstrate that measured strains in principal direction closely followed the strain commands and that transversal compression increased with strain reaching a maximum of $-0.76\% \pm 0.98\%$ at 12% strain (mean \pm SD, $n = 7$). The respective ϵ_y : ϵ_x ratio of 6.3% indicates that strains developed by the LSSE system were largely uniaxial. The dynamic behavior of the system was tested by applying maximal strains ($\epsilon_x = 12\%$) with rise times being shortened from 500 to 50 ms (Figure 2C). Strain plateaus were reached within the predefined rise times and displayed neither overshoots nor creep. Measurements in a further six FCCDs showed that both stretch and relaxation closely followed the command protocols and that strain rates in excess of $\pm 200\% \text{s}^{-1}$ could be achieved (Figure 2D). Overall, the findings demonstrate that the LSSE system follows strain commands with high fidelity and reproducibility and offers strain amplitudes and dynamics that cover the range of values expected to occur *in vivo*.

Precision of 3D target stabilization during variably shaped strain pulses

The efficacy of the LSSE system in stabilizing a defined point on the substrate representing the cell-electrode interface during strain events was tested by applying trains of trapezoidal strain pulses ($\epsilon_x = 12\%$) exhibiting

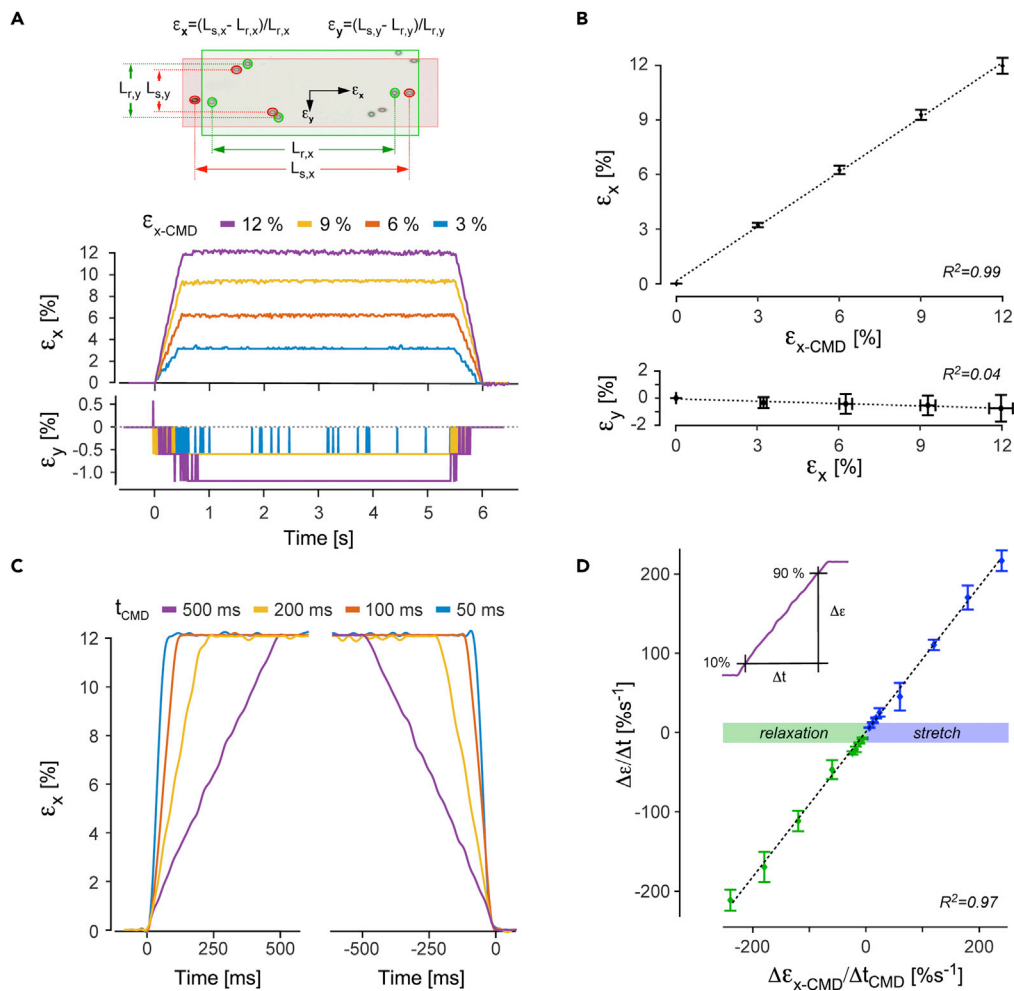


Figure 2. Maximal strain rates and amplitudes provided by the LSSE system

(A) Top: schematic illustration of parameters used to assess in-plane strains ϵ_x and ϵ_y during distension of the FCCD (L_s : length at maximal strain; L_r : length during relaxation). Middle: time course of ϵ_x during application of trapezoidal strains at a fixed rise time of 500 ms and amplitudes of 3%, 6%, 9%, and 12%. Bottom: transversal compression occurring in parallel to the stretch events.

(B) Top: measured principal strains (ϵ_x) versus strain commands (ϵ_{x-CMD}) with stippled line indicating proportionality of the data (mean \pm SD, $n = 28$). Bottom: transverse compressive strain (ϵ_y) plotted against strain in principal direction (ϵ_x) (mean \pm SD, $n = 28$).

(C) Raw strain traces in principal direction (ϵ_x) in response to trapezoidal strain commands exhibiting a constant amplitude of 12% and rise times amounting to 50 (blue), 100 (red), 200 (yellow), and 500 ms (violet).

(D) Plot of measured ($\Delta\epsilon / \Delta t$) versus commanded ($\Delta\epsilon_{x-CMD} / \Delta t_{CMD}$) strain dynamics during stretch and relaxation. Values for $\Delta\epsilon / \Delta t$ were determined as shown by the inset. Stretch and relaxation data (mean \pm SD, $n = 14$) are fitted by a single linear function.

variable rise times to the FCCD. In-plane (x-y) stabilization performance was assessed based on an arbitrarily chosen optical landmark serving as reference point to be stabilized. Of note, this landmark was excluded from the interpolation procedures to simulate a truly random selection of a point to be stabilized within the preparation. Out-of-plane (z) stabilization was tracked with the SICM. Representative raw traces of the positional errors x_e , y_e , and z_e as recorded during single strain pulses are shown in Figure 3A. The data demonstrate that, irrespective of the rise time chosen, in-plane displacements of the landmark during strains were minimal. By contrast, z_e displayed a small offset during the strain plateau that tended to increase with faster rise times. The compilation of positional errors measured every 35 ms during 10 successive strain pulses shown in Figure 3B for a single FCCD indicates that the precision of in-plane and out-of-plane stabilization slightly decreased with increasing strain dynamics. The summary of results obtained from six

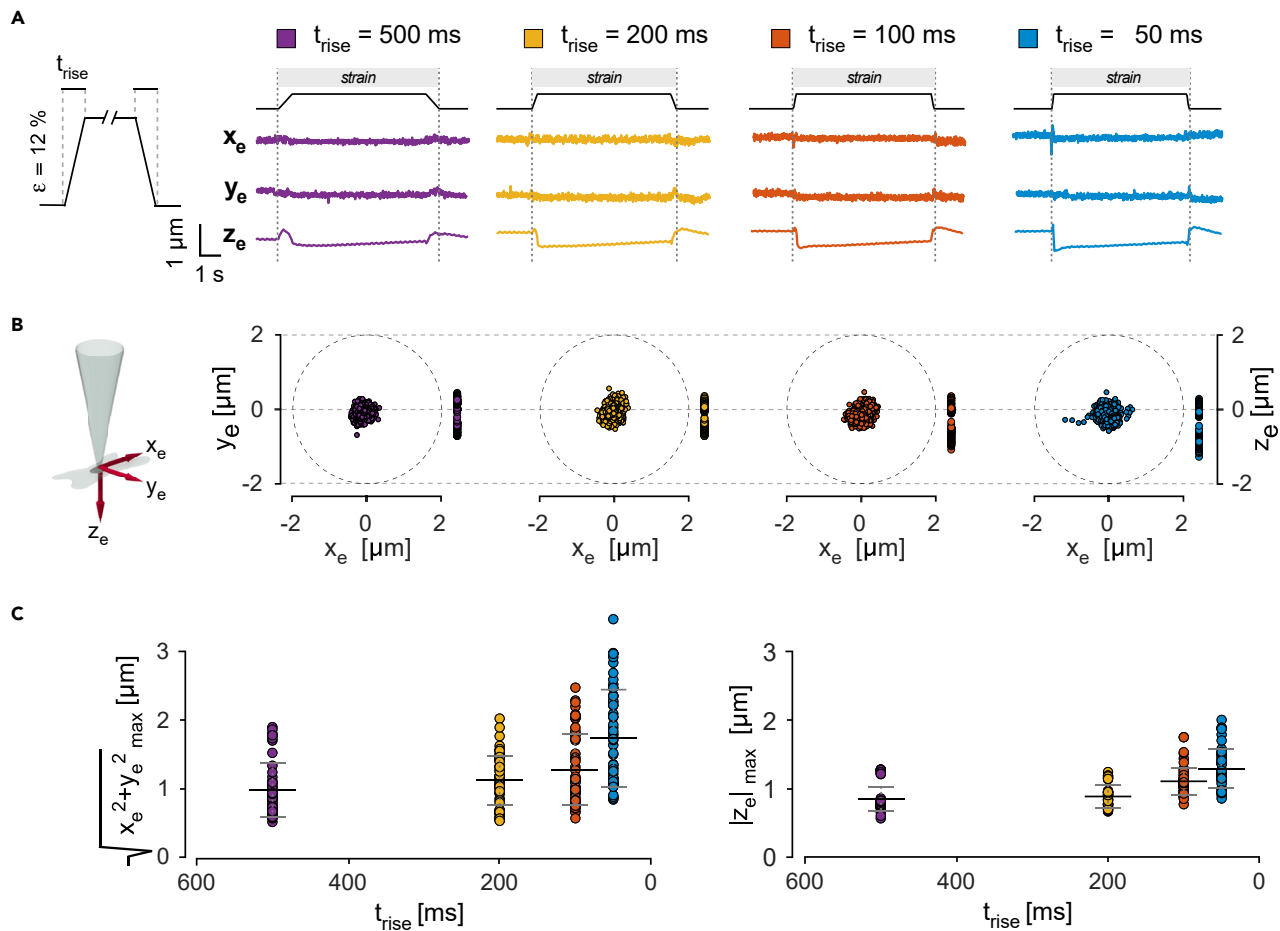


Figure 3. Precision of 3D target stabilization during variably shaped strain pulses

(A) Raw data of positional in-plane (x_e , y_e) and out-of-plane (z_e) errors during application of 5-s-long strain pulses exhibiting a constant amplitude (12%) and rise times ranging from 500 ms down to 50 ms.

(B) Scatterplots of positional errors in respect to a putative gigaseal location (x - y) and the micropipette position (z) as measured during 10 sequential strain pulses conducted with the protocol shown in (A).

(C) Left panel: maxima of Euclidian in-plane displacements for 12% strains applied at indicated rise times (mean \pm SD; 6 devices with 10 strain events each). Right panel: maxima of out-of-plane displacements recorded during the same experiments (absolute values). Horizontal lines indicate mean \pm SD.

different FCCDs subjected to 10 strain events each are shown in Figure 3C. Values correspond to maximal positional errors observed during strain events and are presented either as in-plane Euclidian distances (x , y) or absolute values of out-of-plane displacement (z). The data show that, on average, maximal positional errors during strain events amounted to $\sim 1 \mu\text{m}$ for rise times as fast as 100 ms. At the fastest rise time (50 ms) tested, maximal errors increased to $1.7 \pm 0.7 \mu\text{m}$ (x - y ; $n = 12$) and $1.3 \pm 0.3 \mu\text{m}$ (z ; $n = 12$). Given the result of tests showing that gigaseals tend to be lost when pipette tips are actively displaced by $> 2 \mu\text{m}$ from the initial site of seal formation (data not shown), the point-stabilization performance of the LSSE system can be expected to maintain functional gigaseals during application of 12% strains at rates in excess of 200 \% s^{-1} .

Fidelity of strain transmission to adherent cells

The efficacy of transmitting strain induced in the flexible substrate to adherent cells was tested with cultured single NIH3T3 cells that were labeled with a fluorescent cell membrane probe. As shown in Figure 4A, three different levels of strain (4%, 8%, and 12%) led to an equal amount of cell distension as indicated by the relative change in distance between the two cell extremities along the principal axis. Results obtained using the same strain protocol with an additional 13 NIH3T3 cells (Figure 4B) demonstrated that, on average, the strain-induced cell distension equals the preset strain level and that, at rest, cells resume

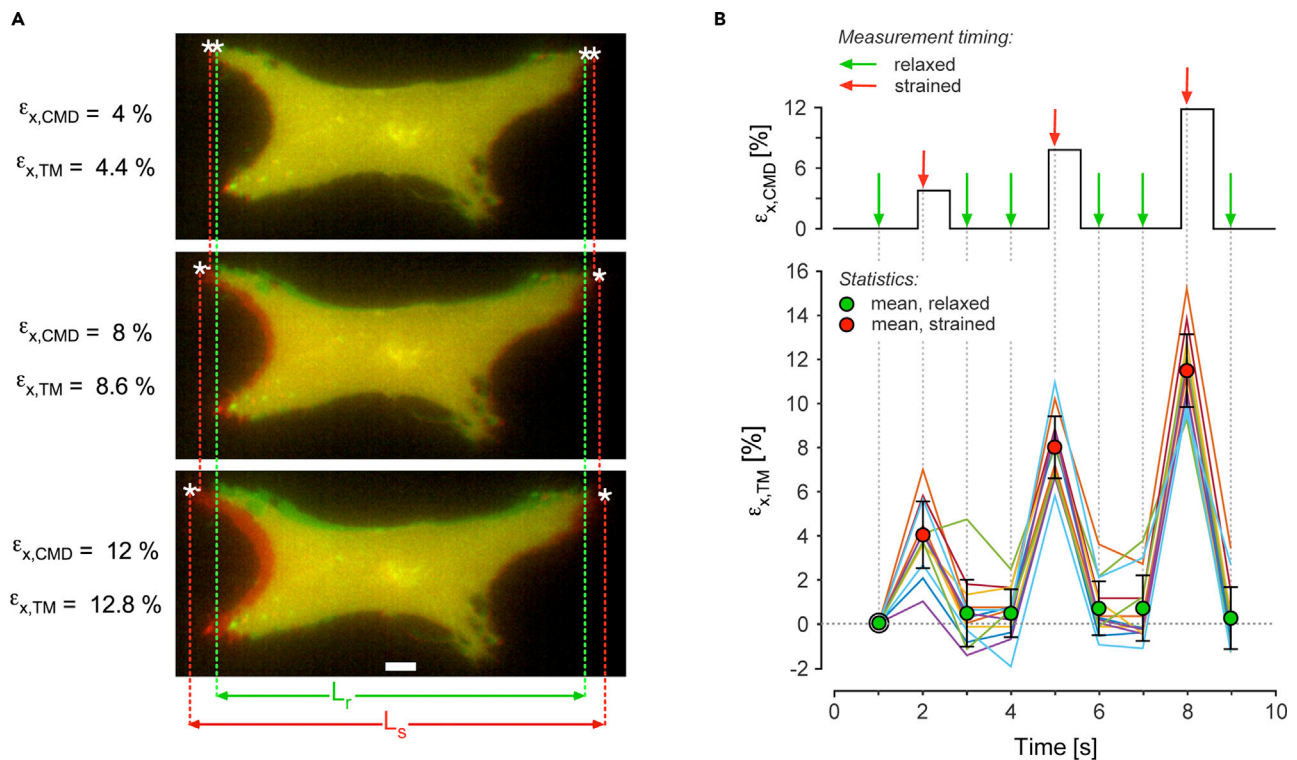


Figure 4. Fidelity of strain transmission to adherent cells

(A) Composite images of an adherent NIH3T3 cell in relaxed state (green) and during strain application ($\epsilon_{x,CMD}$) with amplitudes of 4%, 8%, and 12% in principal direction (red). The transmitted strain ($\epsilon_{x,TM}$) is defined as $(L_s - L_r)/L_r$ (L_r : length at rest; L_s : length during strain). Scale bar, 5 μm . (B) Top: strain protocol with arrows indicating the time when the measurements were performed. Bottom: transmitted strains as measured in 14 individual NIH3T3 cells in 2 devices (green disks: relaxed state; red disks: strained state; mean \pm SD).

their initial configuration with no indication of drift. Overall, the findings demonstrate that strain induced in the flexible substrate is transmitted with high fidelity to adherent cells.

Proof-of-concept measurements: mechanically activated ion currents in NIH3T3 Cells

Proof-of-concept experiments were conducted with NIH3T3 embryonic mouse fibroblast cells that were shown before to exhibit mechanosensitive currents (Chubinskiy-Nadezhdin et al., 2018). Sensitivity to strain was investigated by subjecting the cells to whole-cell voltage-clamp recording (holding potential: -35 mV) and by recording MA currents elicited by strain pulses (rise time: 50 ms, duration: 0.5 s) with strain amplitudes being gradually increased to 12% (Figure 5A). Individual sweeps were preceded by a 12% strain pulse (50 ms rise time; 0.5 s long; not shown) followed by a 120-s-long relaxation period to establish identical initial conditions for each run. As depicted by the lower panel of Figure 5A, strain amplitudes $<6\%$ failed to elicit MA currents. At higher strain amplitudes, MA currents increased drastically and, as shown by the strain-current relationships in Figure 5B, tended to level off in two of five cells at the highest strain amplitudes applied (12%). Eliciting MA currents in the remaining three cells required higher strain amplitudes, and the corresponding current failed to show saturation at the maximal strain amplitudes. The data demonstrate that MA currents of 3T3NIH cells exhibit a threshold behavior with regard to ϵ_x and that, for those cells exhibiting a low threshold, MA currents show a sigmoidal relationship to strain. To characterize the voltage dependence of MA currents of NIH3T3 cells, cells held at -35 mV were stepped for 9 s to test potentials ranging from -50 mV to $+30$ mV (Figure 5C and Video S1). A single strain pulse (ϵ_x : 12%, rise time: 50 ms, duration 0.5 s) was applied 1 s after stepping the cells to the various test potentials. As illustrated by the lower panel of Figure 5C, stepping the cell to different test voltages before strain application induced only small currents. By contrast, the strain pulse itself generated robust currents that showed faster inactivation at positive than at negative test potentials ($+30$ mV: $\tau = 110$ ms; -50 mV: $\tau = 820$ ms) suggesting that the gating of mechanosensitive ion channels underlying the MA currents was affected by transmembrane voltage. The current-to-voltage relationship of the MA current is shown, together with the results of four other cells, in Figure 5D. The reversal potential of the MA current is close to 0 mV (-3.6 ± 4.1 mV, $n = 5$), which suggests that it is

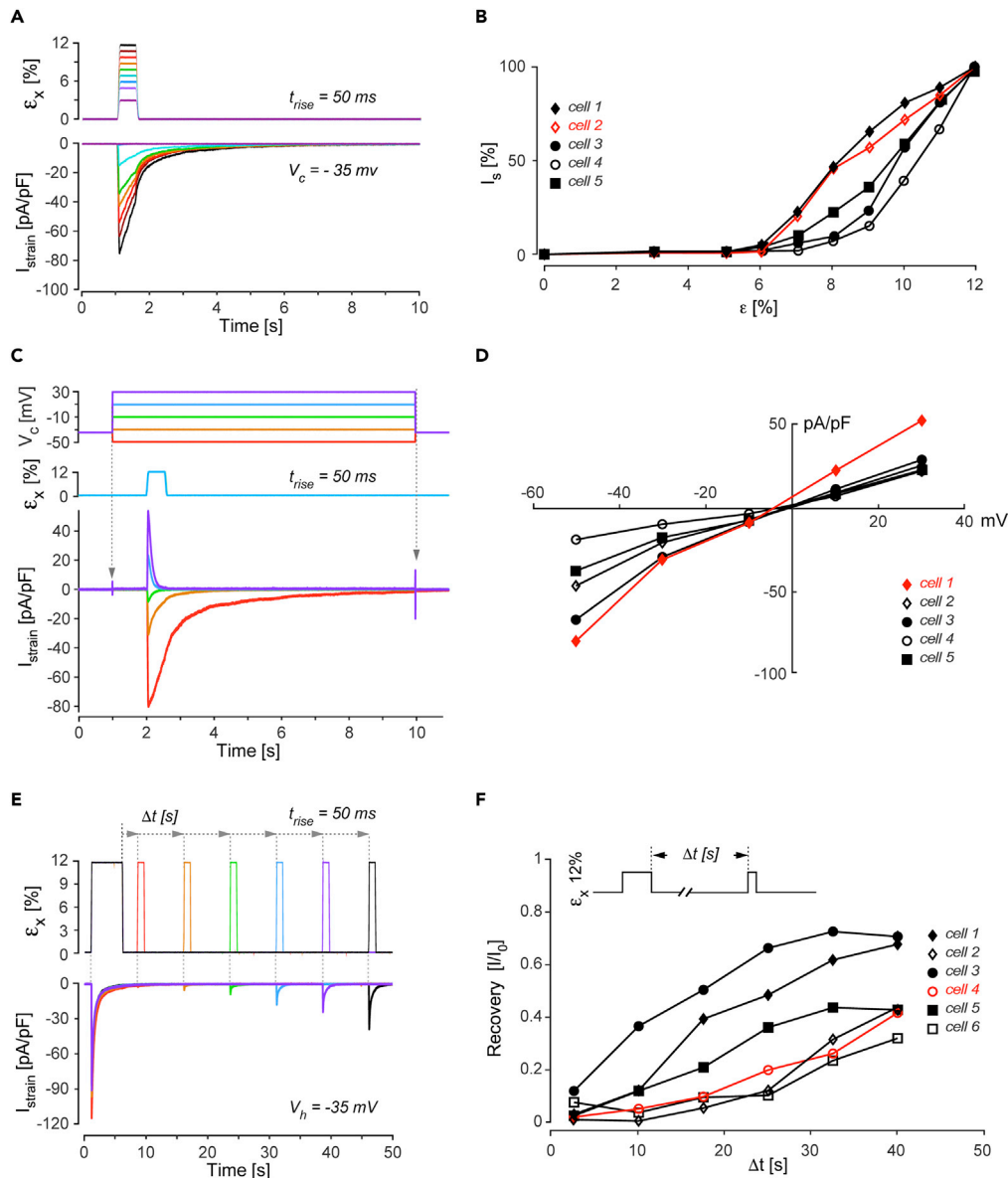


Figure 5. Proof-of-concept measurements: mechanically activated ion currents in NIH3T3 cells

(A) MA current-to-strain relationship for strains ranging from 3% to 12% (upper panel). The strain-induced inward currents are color-coded accordingly (lower panel).

(B) Dependence of strain-induced peak MA current on strain amplitude in five different cells. Evoked MA currents are normalized to MA currents obtained at maximal strain (12%). The highlighted trace corresponds to the cell shown in (A).

(C) Voltage dependence of MA currents. Top: voltage clamp protocol. Middle: strain protocol. Bottom: MA currents recorded at different holding potentials in a single cell.

(D) MA current-to-voltage relationships obtained with the protocol shown in (C) with the data of that particular cell highlighted in red.

(E) To assess recovery from inactivation, cells clamped to -35 mV were subjected to 2-pulse strain protocols with the second strain event being increasingly delayed with respect to the initial strain pulse (upper panel). Inward currents elicited by this protocol are shown in the panel below for a single NIH3T3 cell.

(F) Time-dependent recovery of MA currents as determined by the 2-pulse protocol in five additional cells. Recovery is defined as the ratio of maximal MA currents recorded during strain₂ and strain₁, respectively. The red trace refers to the cell shown in (E).

based on non-selective cation channels. Because pilot experiments with NIH3T3 cells showed that amplitudes of MA currents are highly sensitive to strain pulse intervals, we designed a strain protocol suitable to analyze the time-dependent recovery of MA currents from inactivation. The protocol (Figure 5E) consisted of paired strain pulses with the initial pulse (strain₁; ϵ_x : 12%, rise time: 50 ms, duration 5 s to allow for full inactivation) being followed at increasing delays by the second pulse (strain₂; ϵ_x : 12%, rise time: 50 ms, duration 1 s). Consecutive strain₁-strain₂ protocols were separated by 120 s. As shown in the lower panel of Figure 5E, strain₁ consistently elicited a robust inward current in the voltage clamped cell (holding potential: -35 mV; maximum inward current -95.5 ± 10.2 pA/pF; $n = 6$). By contrast, strain₂ barely induced a current when applied shortly (7.5 s) after the initial pulse. The effectiveness of strain₂ for inducing MA currents increased with increasing strain₁-strain₂ intervals and reached 42% of the initial current at an interval of 40 s. The results obtained from an additional five NIH3T3 cells subjected to the same protocol is shown in Figure 5F. In general, recovery from inactivation of the MA currents was qualitatively similar among cells but showed quantitative differences with two cells recovering >60% of the initial current after ~ 22 and 31 s, respectively, whereas others recovering only 40% or less during the same time interval.

During the experiments shown in Figure 5, individual cells underwent 7 to 28 strain events (17.3 ± 6.9 , mean \pm SD; $n = 11$) that were conducted, in most cases, at maximal amplitudes and strain rates. Individual experiments lasted between 12 and 59 min (27.7 ± 13.5 min, mean \pm SD; $n = 11$) and were actively aborted by the experimenter. The overall success rate of straining cells in whole-cell recording configuration with the LSSE system amounted to 63%, i.e., in 35 of 56 cells undergoing whole-cell recording while being subjected to 14.2 ± 9.1 strain cycles, the gigaseal was maintained during the entire experiment. Examples for a loss of gigaseal integrity associated with strain development and relaxation are depicted in Figure S5.

DISCUSSION

Precision mechanics (Wei et al., 2017), computer vision, and scanning ion-conduction microscopy (Hansma et al., 1989) were integrated into an experimental system that permits continuous measurements of transmembrane currents and membrane potentials of adherent cells undergoing physiological in-plane linear stretch events (Kobirumaki-Shimozawa et al., 2016). The combination of piezo-based real-time feedback (x-y) and feedforward control (z) limited 3D excursions of a fixpoint on a given cell relative to the tip of the patch pipette to $< \pm 2$ μ m during strains up to 12% and strain rates exceeding 200 %s⁻¹. These small excursions were tolerated by the gigaseals formed by the pipette on the cells as demonstrated by an overall success rate of >60% for performing multiple strain experiments on individual cells without losing gigaseal integrity (cf. Video S1). The LSSE system delivered highly reproducible strain magnitudes and dynamics thereby enabling a systematic characterization of the cellular response to predefined strains that closely reproduces physiological stretch and relaxation events with regard to amplitude, rate, and directionality. Offering uniaxial strains not only permits to probe cells being normally exposed to such strains *in vivo* but opens the perspective to systematically investigate the effect of strain directionality on mechanosensitivity of cells exhibiting a polar organization of their cytoskeleton. If biaxial strains should be of interest, the open design of the LSSE permits the introduction of a further strain axis by appropriate modification of the hardware.

Proof-of-concept recordings with NIH3T3 cells showed robust strain-induced inward currents when cells were clamped to their resting membrane potential (Chen et al., 1988; De Simone et al., 2020). At $\epsilon \geq 6\%$, MA currents increased with increasing strain amplitudes with some signals showing a sigmoidal dependence on strain, whereas others failed to saturate at the maximal strain levels provided by the LSSE system. The observation of a strain threshold for MA currents may be explained by the presence of membrane slackness under control conditions that needed to be overcome until activation of mechanosensitive ion channels set in. An activation threshold for MA currents has been described before in cell indentation experiments (Anderson et al., 2018; Romero et al., 2019; Shin et al., 2019; Taberner et al., 2019). To which extent these findings compare with our results cannot be decided because indentation depths cannot be directly correlated to cell deformation. The close to linear current-to-voltage relationships of MA currents of NIH3T3 cells suggests that they were primarily carried by mechanosensitive non-selective cation channels (Ranade et al., 2015). Shortly after onset of strain, MA currents inactivated with voltage-dependent kinetics. Contrary to what was reported before for Piezo 1 and Piezo 2 channels, the time constants of inactivation at negative potentials were longer than those at positive potentials (Coste et al., 2010). Moreover, double-strain protocols showed that NIH3T3 cell MA currents recovered only slowly from inactivation requiring in excess of 2 min until full initial sensitivity was restored, which further distinguishes the observed MA currents from piezo-dependent currents (Lewis and Grandl, 2020). Alternatively, the MA currents observed may have been carried by mechanosensitive TRP channels (Inoue et al., 2009; Liu and Montell, 2015). A direct

comparison of our findings to previous characterizations of mechanosensitive TRP channels has to be done with caution because earlier data describing the kinetics of voltage-dependent inactivation or recovery from inactivation were obtained using non-quantitative straining methods or highly localized mechanical stimuli delivered by nanopillars (Servin-Vences et al., 2017). Moreover, it needs mentioning that there is an ongoing debate whether TRP channels are mechanosensitive (Nikolaev et al., 2019). In summary, the precise molecular basis of the MA currents observed during our proof-of-concept measurements with NIH3T3 cells as well as the precise mechanisms underlying their threshold behavior remain to be elucidated.

In summary, the LSSE system presented enables application of defined linear strains to entire adherent cells undergoing simultaneously whole-cell patch clamp recording. As strains are exactly defined in space and time, results obtained with the system not only permit a direct comparison of results obtained with different cell types but also allow gaining standardized functional signatures of the many different types of mechanosensitive ion channels thereby contributing to the establishment of a systematic foundation of the function of these channels in both health and disease.

Limitations of the study

Limitations of the LSSE system concern the circumstance that, so far, only adherent cell types can be investigated. Firmly attaching other cell types like freshly isolated rod-shaped cardiomyocytes to the substrate with adhesive compounds like Cell-Tak have not been successful (data not shown). In this context, further developments are necessary to expand the use of the LSSE system to non-adherent cell types. Also, strain and strain rates, even though covering most of the physiological range, are presently limited to 12% and $240\text{ }\mu\text{s}^{-1}$, respectively. If required, however, this range can be extended by increasing the precision and response time of the feedback stabilization processes. Furthermore, the LSSE system incorporates a full SICM microscope. In future builds, the system may be simplified by removing the x-y NPs of the SICM head. Alternatively, the SICM system may be retained for obtaining 3D scans of the cell surface under different strain conditions. In future applications, the LSSE system may be combined with fluorescence-based force/tension sensor technology (Guo et al., 2014) to relate MA currents not only to overall cellular strain but also to mechanical stress fields within the cell membrane.

Resource availability

Lead contact

Further information and requests should be directed to and will be fulfilled by Prof. Stephan Rohr (stephan.rohr@unibe.ch).

Materials availability

This study did not generate new unique reagents.

Data and code availability

The original unprocessed data and electrophysiological recordings are available upon request to the corresponding authors.

METHODS

All methods can be found in the accompanying [Transparent Methods supplemental file](#).

SUPPLEMENTAL INFORMATION

Supplemental Information can be found online at <https://doi.org/10.1016/j.isci.2021.102041>.

ACKNOWLEDGMENTS

This research was supported by a grant of the Swiss National Science Foundation (no. 310030_169234 to S.R.). We greatly acknowledge the excellent cell culture work by Ms. Regula Flückiger-Labrada and the help of A. Nomura, MD, with the Cell-Tak experiments and Georg Rohr for producing the graphical abstract.

AUTHOR CONTRIBUTIONS

S.R. and E.d.C. conceptualized the method. E.d.C. designed and implemented the stretch device, the control system, and the high-voltage amplifiers. C.D. designed and implemented the custom SICM electronics

with control software and the low-noise power supply for the high-voltage amplifiers. E.d.C. performed the experiments and data analysis. E.d.C. and S.R. wrote the manuscript.

DECLARATION OF INTERESTS

The authors declare no competing interests.

Received: November 2, 2020

Revised: December 3, 2020

Accepted: January 4, 2021

Published: February 19, 2021

REFERENCES

- Anderson, E.O., Schneider, E.R., Matson, J.D., Gracheva, E.O., and Bagriantsev, S.N. (2018). TMEM150C/Tentonin3 is a regulator of mechano-gated ion channels. *Cell Rep.* 23, 701–708.
- Besch, S.R., Suchyna, T., and Sachs, F. (2002). High-speed pressure clamp. *Pflugers Arch.* 445, 161–166.
- Carreon, T.A., Castellanos, A., Gasull, X., and Bhattacharya, S.K. (2017). Interaction of cochlin and mechanosensitive channel TREK-1 in trabecular meshwork cells influences the regulation of intraocular pressure. *Sci. Rep.* 7, 452.
- Chen, C.F., Corbley, M.J., Roberts, T.M., and Hess, P. (1988). Voltage-sensitive calcium channels in normal and transformed 3T3 fibroblasts. *Science* 239, 1024–1026.
- Chubinskiy-Nadezhdin, V.I., Efremova, T.N., Negulyaev, Y.A., and Morachevskaya, E.A. (2018). Coupled activation of mechanosensitive and calcium-dependent potassium channels in 3T3 and 3T3-SV40 cells. *Cell Tissue Biol.* 12, 231–237.
- Coste, B., Mathur, J., Schmidt, M., Earley, T.J., Ranade, S., Petrus, M.J., Dubin, A.E., and Patapoutian, A. (2010). Piezo1 and Piezo2 are essential components of distinct mechanically activated cation channels. *Science* 330, 55–60.
- De Simone, S.A., Moyle, S., Buccarello, A., Dellenbach, C., Kucera, J.P., and Rohr, S. (2020). The role of membrane capacitance in cardiac impulse conduction: an optogenetic study with non-excitable cells coupled to cardiomyocytes. *Front. Physiol.* 11, 194.
- Ferraiuoli, P., Kappler, B., van Tuijl, S., Stijnen, M., de Mol, B., Fenner, J.W., and Narracott, A.J. (2019). Full-field analysis of epicardial strain in an in vitro porcine heart platform. *J. Mech. Behav. Biomed. Mater.* 91, 294–300.
- Gordon, E., Schimmel, L., and Frye, M. (2020). The importance of mechanical forces for in vitro endothelial cell biology. *Front. Physiol.* 11, 684.
- Guharay, F., and Sachs, F. (1984). Stretch-activated single ion channel currents in tissue-cultured embryonic chick skeletal muscle. *J. Physiol.* 352, 685–701.
- Guo, J., Sachs, F., and Meng, F. (2014). Fluorescence-based force/tension sensors: a novel tool to visualize mechanical forces in structural proteins in live cells. *Antioxid. Redox Signal.* 20, 986–999.
- Hansma, P., Drake, B., Marti, O., Gould, S., and Prater, C. (1989). The scanning ion-conductance microscope. *Science* 243, 641–643.
- Hao, J., and Delmas, P. (2011). Recording of mechanosensitive currents using piezoelectrically driven mechanostimulator. *Nat. Protoc.* 6, 979–990.
- Inoue, R., Jian, Z., and Kawarabayashi, Y. (2009). Mechanosensitive TRP channels in cardiovascular pathophysiology. *Pharmacol. Ther.* 123, 371–385.
- Janmey, P.A., Fletcher, D.A., and Reinhart-King, C.A. (2020). Stiffness sensing by cells. *Physiol. Rev.* 100, 695–724.
- Kobirumaki-Shimozawa, F., Oyama, K., Shimozawa, T., Mizuno, A., Ohki, T., Terui, T., Minamisawa, S., Ishiwata, S.I., and Fukuda, N. (2016). Nano-imaging of the beating mouse heart in vivo: importance of sarcomere dynamics, as opposed to sarcomere length per se, in the regulation of cardiac function. *J. Gen. Physiol.* 147, 53–62.
- Lewis, A.H., and Grandl, J. (2020). Inactivation kinetics and mechanical gating of Piezo1 ion channels depend on subdomains within the cap. *Cell Rep.* 30, 870–880.e872.
- Liu, C., and Montell, C. (2015). Forcing open TRP channels: mechanical gating as a unifying activation mechanism. *Biochem. Biophys. Res. Commun.* 460, 22–25.
- McCarter, G.C., Reichling, D.B., and Levine, J.D. (1999). Mechanical transduction by rat dorsal root ganglion neurons in vitro. *Neurosci. Lett.* 273, 179–182.
- Nikolaev, Y.A., Cox, C.D., Ridone, P., Rohde, P.R., Cordero-Morales, J.F., Vásquez, V., Laver, D.R., and Martinac, B. (2019). Mammalian TRP ion channels are insensitive to membrane stretch. *J. Cell Sci.* 132, jcs238360.
- Numata, T., Shimizu, T., and Okada, Y. (2007). Direct mechano-stress sensitivity of TRPM7 channel. *Cell. Physiol. Biochem.* 19, 1–8.
- Olesen, S.P., Clapham, D.E., and Davies, P.F. (1988). Haemodynamic shear stress activates a K⁺ current in vascular endothelial cells. *Nature* 331, 168–170.
- Poole, K., Herget, R., Lapatsina, L., Ngo, H.D., and Lewin, G.R. (2014). Tuning Piezo ion channels to detect molecular-scale movements relevant for fine touch. *Nat. Commun.* 5, 3520.
- Quinn, T.A., and Kohl, P. (2021). Cardiac mechano-electric coupling: acute effects of mechanical stimulation on heart rate and rhythm. *Physiol. Rev.* 101, 37–92.
- Quinn, T.A., Kohl, P., and Ravens, U. (2014). Cardiac mechano-electric coupling research: fifty years of progress and scientific innovation. *Prog. Biophys. Mol. Biol.* 115, 71–75.
- Ranade, S.S., Syeda, R., and Patapoutian, A. (2015). Mechanically activated ion channels. *Neuron* 87, 1162–1179.
- Romero, L.O., Massey, A.E., Mata-Daboin, A.D., Sierra-Valdez, F.J., Chauhan, S.C., Cordero-Morales, J.F., and Vasquez, V. (2019). Dietary fatty acids fine-tune Piezo1 mechanical response. *Nat. Commun.* 10, 1200.
- Sachs, F. (2015). Mechanical transduction by ion channels: a cautionary tale. *World J. Neurol.* 5, 74–87.
- Sachs, F. (2018). Mechanical transduction and the dark energy of biology. *Biophysical J.* 114, 3–9.
- Servin-Vences, M.R., Moroni, M., Lewin, G.R., and Poole, K. (2017). Direct measurement of TRPV4 and PIEZO1 activity reveals multiple mechanotransduction pathways in chondrocytes. *Elife* 6, e21074.
- Shin, K.C., Park, H.J., Kim, J.G., Lee, I.H., Cho, H., Park, C., Sung, T.S., Koh, S.D., Park, S.W., and Bae, Y.M. (2019). The Piezo2 ion channel is mechanically activated by low-threshold positive pressure. *Sci. Rep.* 9, 6446.
- Taberner, F.J., Prato, V., Schaefer, I., Schrenk-Siemens, K., Heppenstall, P.A., and Lechner, S.G. (2019). Structure-guided examination of the mechanogating mechanism of PIEZO2. *Proc. Natl. Acad. Sci. U S A* 116, 14260–14269.
- Wei, H., Shirinzadeh, B., Li, W., Clark, L., Pinski, J., and Wang, Y. (2017). Development of piezo-driven compliant bridge mechanisms: general analytical equations and optimization of displacement amplification. *Micromachines* 8, 238.

Supplemental Information

**Advancing mechanobiology by performing whole-cell
patch clamp recording on mechanosensitive cells
subjected simultaneously to dynamic stretch events**

Etienne de Coulon, Christian Dellenbach, and Stephan Rohr

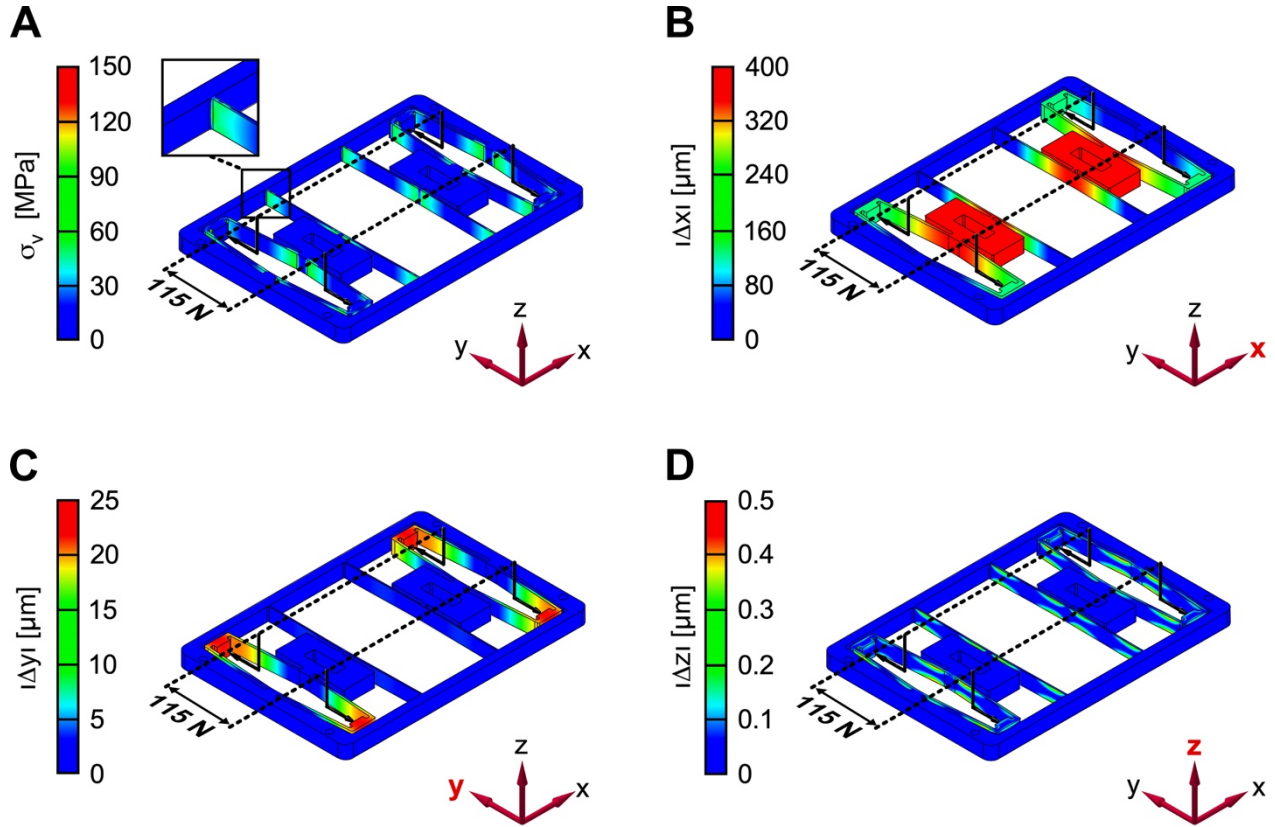
Supplemental Information

Contents

| | |
|-----------|--|
| Figure S1 | Finite Element Analysis (FEA) of the Kinematic Structure of the Strain Stage |
| Figure S2 | Strain Stage Control |
| Figure S3 | In-plane Real-time Video Feedback Stabilization |
| Figure S4 | Feedforward Calibration and Compensation of Strain-Induced z-axis Displacements |
| Figure S5 | Examples for Strain-Associated Loss of Gigaseal Integrity |

Transparent Methods

Figure S1. Finite Element Analysis (FEA) of the Kinematic Structure of the Strain Stage, Related to Figure 1.



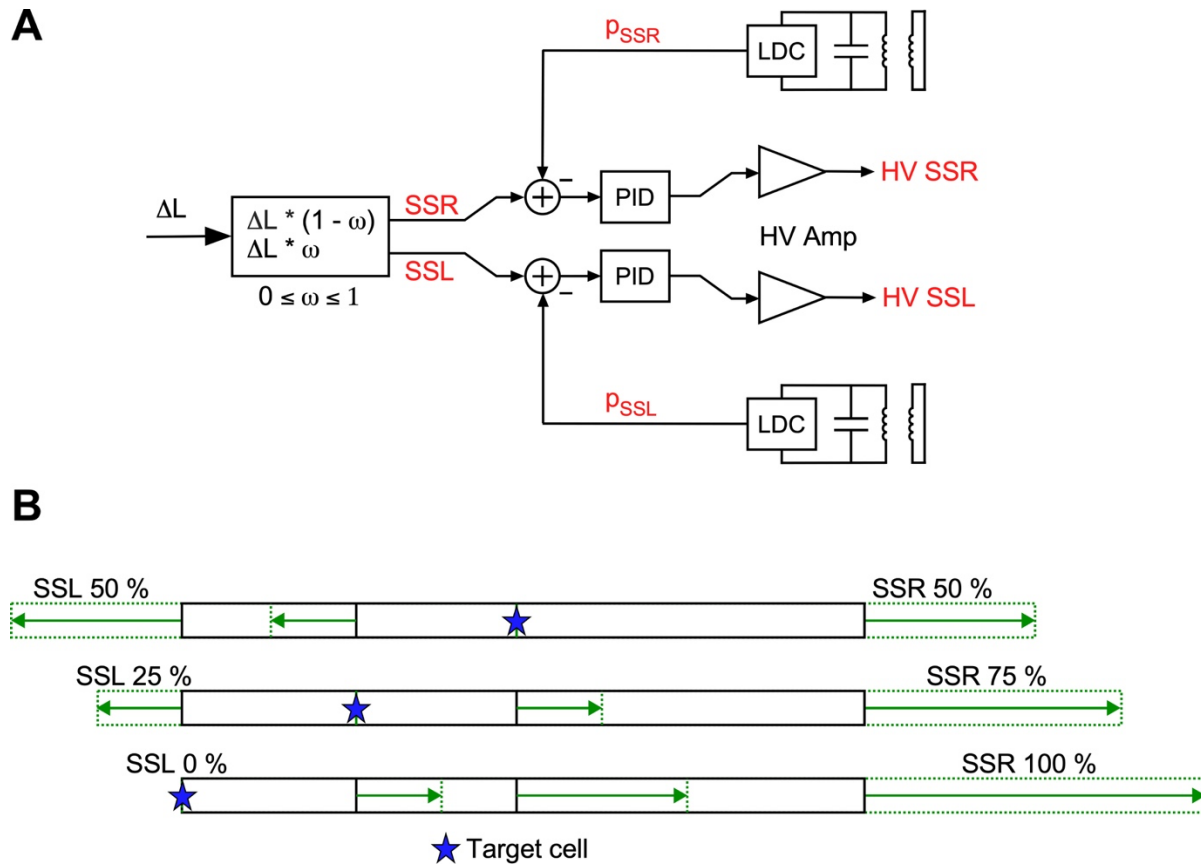
(A) FEA of the von Mises stress (σ_v) resulting from a 115 N force input at the piezo stack interface (black arrows). For the titanium alloy used (Ti-6Al-4V), a structure is considered fatigue-proof, if σ_v stays below 400 MPa.

(B) FEA of the displacement in x-direction resulting from 115 N force input at the piezo stack interface. The force induces each stage to move by 400 μm in lateral direction (x) thereby extending the central deformable gap of the flexible cell culture dish, once mounted, from 2 mm to 2.8 mm (40 % strain).

(C) In sagittal direction (y), application of 115 N force causes a movement of 25 μm to each side with a spring constant of 115 N / 50 μm = 2.3 $\text{N}\mu\text{m}^{-1}$. The ratio of lateral (400 μm) and sagittal (25 μm) stage movement in presence of 115 N force results in a mechanical gain factor of the actuator stroke of 16.

(D) FEA of the displacement in z-direction resulting from 115 N force input at the piezo stack interface confirms that there is only minimal out-of-plane parasitic displacement during activation of the structure.

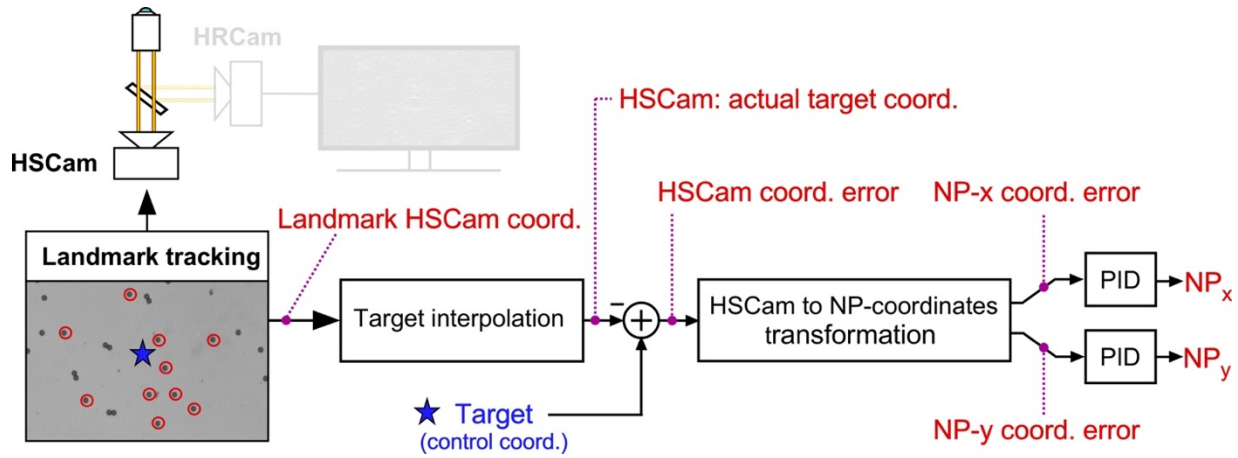
Figure S2. Strain Stage Control, Related to Figure 1.



(A) Block-diagram of the strain stage (SS) control. The global set-point, ΔL , and the absolute expansion needed to achieve the desired strain, ϵ , are distributed among the two antiparallel axes, SS-left (SSL) and SS-right (SSR), by the weighting factor ω . This factor is chosen such that a prospective pipette target location on a cell in the microscopic field of view stays roughly in place when strain is applied. The process determines two individual set-points, SSL and SSR, for each axis which are compared against the actual position (p_{SSL} and p_{SSR}) provided by the inductive displacement sensor. The resulting error signal is fed to a proportional–integral–derivative controller (PID) that drives the custom-made high voltage amplifier (0 to 150 V) controlling the piezo stack actuators of each axis (HV SSL and HV SSR).

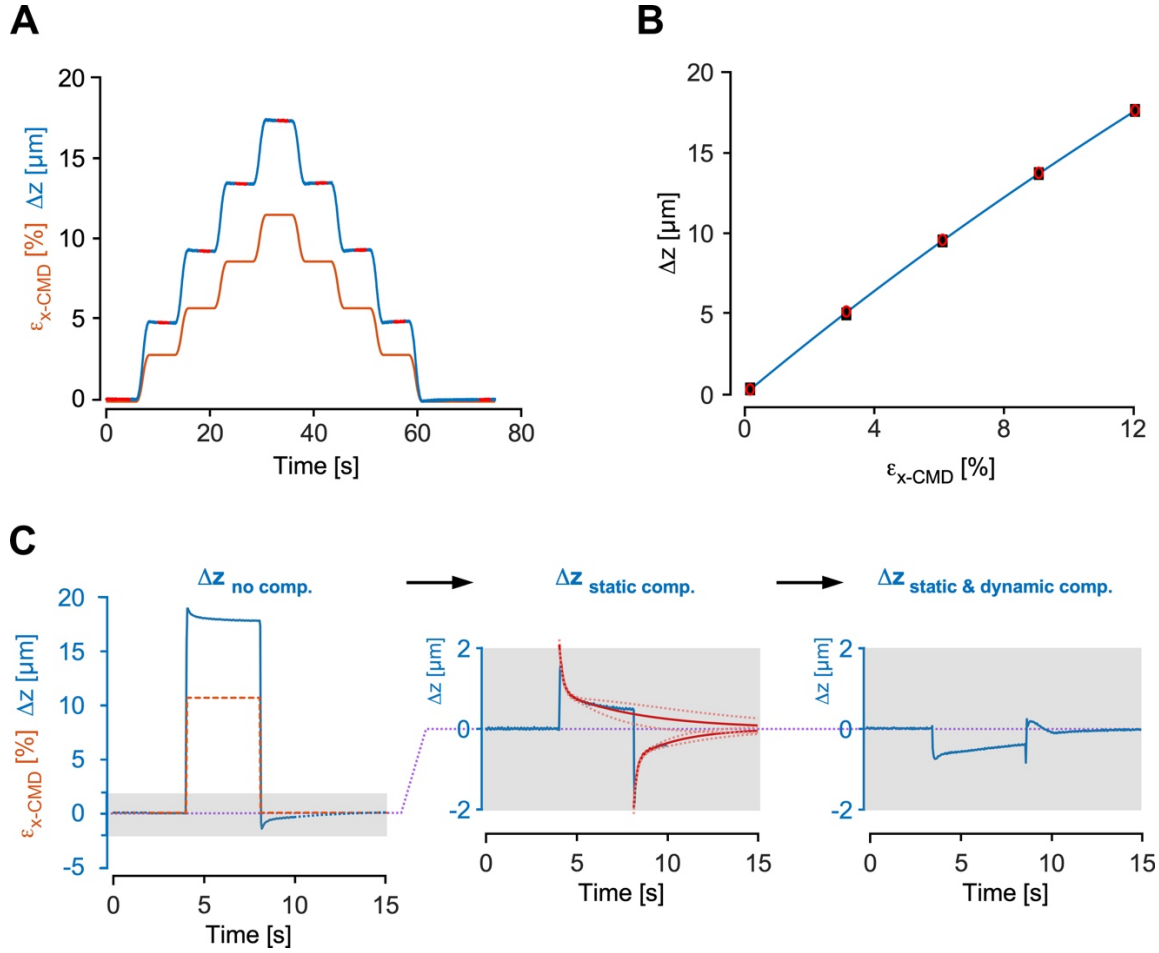
(B) Schematic illustration of how SSL vs. SSR balancing stabilizes a target location (green star) during strain application. In case of a central location of the target, applying symmetric strain to SSL and SSR keeps the point fixed in space. In case where the target is located at 25% of the entire length of the preparation, assigning 25% strain to SSL and 75% strain to SSR equally stabilizes the target. The weights are shifted to 0% (SSL) and 100% (SSR) in case of a target being located at the left end of the flexible substrate.

Figure S3. In-plane Real-time Video Feedback Stabilization, Related to Figure 1.



Based on the actual positions of the landmarks in high-speed camera image coordinates (HSCam coord.), the position of the target to be stabilized during strain events is interpolated. The error vector is then computed by subtraction of the actual target position from the desired target position (control coord.). Subsequently, the error vector is transformed into the coordinate system of the nanopositioner (NP). The x- and y-components of the error vector are fed through a proportional–integral–derivative (PID) controller to actuate the respective NP axes. Positioning is continuously monitored and readjusted at 200 Hz.

Figure S4. Feedforward Calibration and Compensation of Strain-Induced z-axis Displacements,
Related to Figure 1.

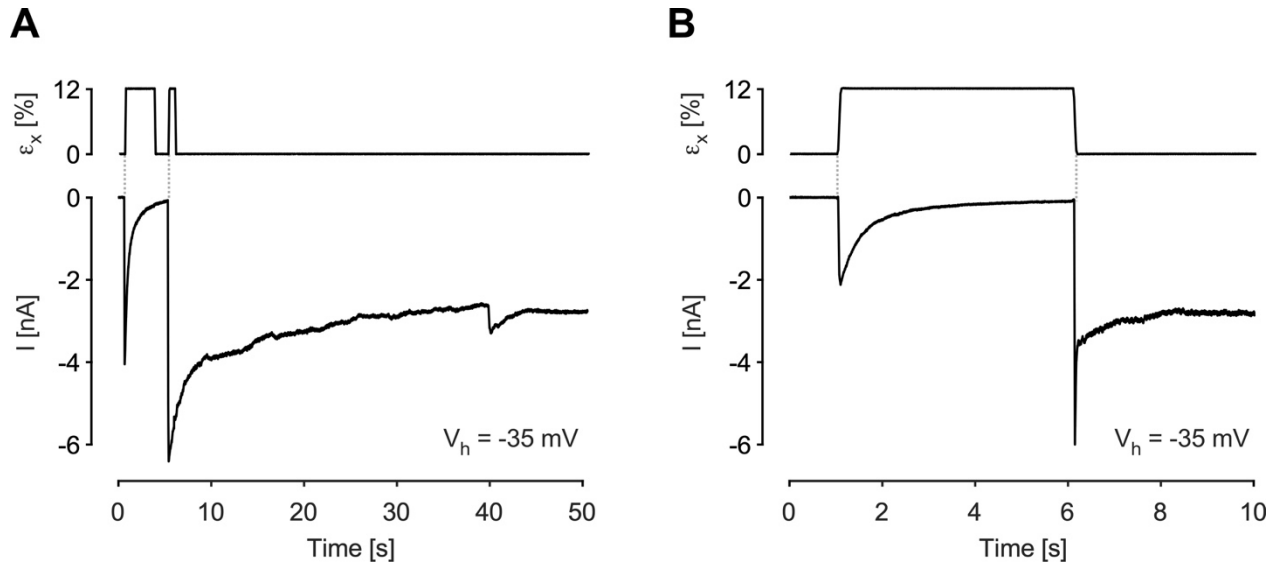


(A) Test protocol (orange) used to assess the static system response in z-direction: x-axis strain is increased in a stepwise fashion followed by a symmetrical decrease while the accompanying z-displacement (blue) is continuously measured by the SICM system.

(B) Plot of measured z-displacements (values: mean of red data points in panel a) vs. commanded strain (red circles: data from ascending limb of the strain waveform; black squares; data from descending limb). The blue line corresponds to the second order polynomial fit of the data.

(C) Feed-forward z-displacement compensation. Left panel: uncompensated z-displacement (blue trace) in response to a maximal strain pulse (stippled orange line; $\epsilon = 12\%$, $t_{\text{rise}} = 50\text{ ms}$). Middle panel: z-displacement (blue trace) after compensation for the static component is characterized primarily by dynamic displacements associated with the onset and conclusion of the strain event. Both phases are fitted with two-term exponentials (solid red lines; stippled red line = 95% confidence intervals) that are used to compensate the dynamic components. Right panel: the combination of static and dynamic compensation results in a final z-displacement $< 1\text{ }\mu\text{m}$ for the 12 % strain pulse applied.

Figure S5. Examples for Strain-Associated Loss of Gigaseal Integrity, Related to Figure 5.



(A) Gigaseal failure during execution of a 2-pulse protocol ($\epsilon = 12\%$, $t_{\text{rise}} = 50$ ms; upper panel). After successful execution of the first pulse, the gigaseal is ruptured during the second pull as indicated by the failure of the transmembrane current to return to 0 (lower panel).

(B) Gigaseal failure during relaxation following a single pulse strain protocol ($\epsilon = 12\%$, $t_{\text{rise}} = 50$ ms). Panel layout as in (A).

Transparent Methods

Kinematic structure of the LSSE system. The kinematic structure of the LSSE was designed and optimized using CAD and finite element analysis (FEA) simulations (AutoCad, Inventor 2015). The final design of the stretcher was manufactured from high performance titanium (Ti-6Al-4V) by electric discharge machining (Argotec AG). Two piezo stack actuators (Thorlabs, PK4FXP2) drive the kinematic structure with the respective FEA being shown in Figure S1. Inductive displacement sensing was implemented using a single chip solution (Texas Instrument, LDC1614) integrated into a custom designed PCB (Altium Limited, Altium Designer, V16.0.6).

FCCD assembly. Two coverslips (25.5 mm x 27 mm; thickness No. 4; Marienfeld GmbH) were collinearly aligned and spaced 1 mm apart using a gauge. A silicone membrane with a thickness of 50 μm (Wacker, Elastosil 20/50) was air-plasma bonded to the coverslips (Harrik, PDC - 32; 30 s treatment at 2 mBar using 18 W of RF power). After bonding, the spacing between the two coverslips was increased to 2 mm using a second gauge and the glasses fixed in place. The bottom side of this subassembly was sprayed with an airbrush (Evolution Silverline Solo 0.2; Harder & Steenbeck) using suitably diluted black dyed polystyrene microspheres (Polysciences, 24239-5) having a diameter of 6 μm . In a separate step, the compliant cell culture well was cast from polydimethylsiloxane (PDMS; Dow Corning, Sylgard 184) using a custom printed 3D mold (Proform AG) made of Accura Xtreme (3D Systems). In a final step, the culture well was bonded to the membrane-glass subassembly using PDMS.

Spatial stabilization system: hardware. 3D displacements during strain events were compensated in real-time by a 3-axis nanopositioning stage (Physik Instrumente, P-545.3R7) connected to a dedicated controller (Physik Instrumente, E-545.3RD) (*c.f. Figure 1 of the article*). The spatial stabilization system was controlled by a standard desktop PC using software written in C++ under inclusion of a real-time computer vision library (Intel Corporation, OpenCV). Image sequences used for the video feedback control were captured with a high-speed camera (200 Hz; Mikrotрон, EoSens CL MC1362) connected by a CameraLink interface to a frame grabber (Silicon Software, microEnable IV VD4-CL). Outgoing control signals were generated by a multifunction DAQ PCI-card (National Instruments, NI PCI-6259) that was connected to two breakout boxes (National Instruments, BNC-2111). The SICM scan head was used to record z-displacements during test strains in order to produce feed-forward protocols to be used during the actual experiments. The scan head consisted of an x-y-z nanopositioning stage (Physik Instrumente, P-621.2CL and P-621.ZCL). The nanopositioners were controlled by dedicated electronics (Physik Instrumente, E-501K025). A micro-translation stage (Physik Instrumente, M-112.1DG) driven by a stepper-motor controller (Physik Instrumente, Mercury C-863) permitted coarse z-translation of the SICM scan head (*for an illustration of the hardware cf. Figure 1 of the article*).

Spatial in-plane stabilization: procedures. Before starting an experiment, the relative excursions of the two antiparallel axes of the strain stage (SSL and SSR) were balanced such that the target location, i.e., the prospective site of gigaseal formation on the cell, underwent minimal lateral shift during strain application (Figure S2). This balancing was achieved by applying a sinusoidal strain pattern (4 % strain, 0.5 Hz) to the substrate while adjusting the SSL vs. SSR excursion such that, visually, the target location roughly retained its position during strain development. The relative excursions of SSL and SSR were controlled using a proportional–integral–derivative controller (PID, Figure S2) that worked under closed-loop control with the

absolute positions of SSL and SSR being provided by the inductive displacement sensor. The output of the PID was connected to two custom made high voltage amplifiers (0 to 150 V) that controlled the piezo stack actuators of each axis (HV SSL and HV SSR). Appropriate balancing of the relative excursions of SSR and SSL permitted turning every point along the axis of principal strain into a 'fixed' point during strain application. High precision in-plane stabilization during ongoing strain events was achieved using real-time video feedback control (Figure S3). For this purpose, optical landmarks formed by the black polystyrene beads were continuously detected at high speed (200 Hz) by normalized cross-correlation of a landmark template image with each video frame. The detected landmarks were tracked from frame to frame and the actual position of the point to be stabilized was continuously inferred by interpolating its position in respect to the tracked landmarks. The difference between the desired and the actual position of the point to be stabilized defined an error vector that was transformed from HSCam coordinates to NP coordinates and used to drive the NP_x and NP_y compensation axes.

Spatial out-of-plane stabilization: procedures. Z-axis stabilization was achieved using a feed-forward compensation that was based, for each individual FCCD, on pre-experimental recordings of z-displacement characteristics as generated by the z-output of the SICM during application of test strains. The test waveform used to drive the SS is shown in Figure S4a. It was based on a stepwise increase of strain to 12 % in steps of 3 % followed by a symmetrical decrease. Measured z-displacements were plotted as a function of strain for both the ascending and descending limb of the stepped strain. As shown in Figure S4b, data from both limbs closely matched each other for a given step height indicating that, irrespective of the strain phase, static z-displacements were reproducibly linked to the strain amplitude. Z-displacement vs. strain amplitude values were fitted by a second order polynomial that served compensation of strain induced static z-displacements during the experiments as shown in Figure S4c. Dynamic z-displacements persisting after compensation of the static component was compensated by fitting a two-term exponential function to both the stretch and relaxation phase of the strain. This component was then added to the static compensation values and used in feed-forward mode for full compensation of z-displacements during strain pulses during the experiments.

Cell culture. NIH3T3 cells (Y. Zimmer lab, DBMR, University of Bern) were kept in DMEM (Sigma, 5671) supplemented with 2 mmol/L L-glutamin (Sigma, G 7513), 1 mmol/L sodium pyruvate (Sigma, S 8636), 10 U/mL penicillin (Sigma, P 7794) and 10 % FCS (Biochrom / Bioswisstec, S 0113). Cells were cultured in T-25 flasks (Vitaris, 3289-COR) at 37 °C in a humid atmosphere containing 5 % CO₂ and were split when reaching 80 % confluency. For experiments, NIH3T3 cells were detached using trypsin (0.05 %) - EDTA (0.02 %) solution (Sigma, 59417C) and resuspended in medium M199 with Hank's salts (Sigma, M7653) that was supplemented with 2 mmol/L L-glutamin (Sigma, G 7513), 2 µg/ml vitamin B₁₂(Sigma, V2876), 20 U/mL penicillin (Sigma, P 7794) and 10 % neonatal calf serum (Biochrom, Bioswisstec, S0125). Prior to cell seeding, FCCD substrates were activated using air-plasma (Harrik, PDC - 32; 30 s treatment at 2 mBar using 18 W of RF power) and subsequently coated with collagen type I (Sigma, C7661). Resuspended NIH3T3 cells were counted with a hemocytometer and diluted with supplemented M199 such as to result in a final density of 100 cells per mm² when seeded into the FCCDs. Two hours post-seeding, the cultures were washed with supplemented M199 containing a reduced amount of serum (5 %). FCCD preparations were kept in an incubator at 36 °C in a humid atmosphere containing 0.8 % CO₂ until being used in experiments 24 h to 48 h after cell seeding.

Patch clamp recordings. Electrophysiological experiments using standard whole-cell patch clamp recording techniques were conducted at room temperature after mounting the FCCDs into the LSSE system that was placed on an inverted microscope (Zeiss, Axiovert 35M) equipped for epifluorescence. Prior to the experiments, the culture medium was exchanged with Hank's buffered saline solution (HBSS; AppliChem, A3140) that contained 10 mmol/L Hepes (Sigma, 5467) titrated to pH = 7.40 with 1 M NaOH. Patch pipettes were pulled from borosilicate glass capillaries (GC150F-10, Harvard Apparatus) with a filament puller (Zeitz, DMZ universal Puller). The patch pipette filling solution contained (in mmol/L) K-aspartate 120, NaCl 10, MgATP 3, CaCl₂ 1, EGTA 10 and HEPES 5 (pH 7.2; calculated free Ca²⁺ concentration of ~ 35 nmol/L). Pipette resistances ranged from 4 to 7 MΩ. Pipette potentials were zeroed before cell contact and measured potentials were corrected for the liquid junction potential (12.4 mV) as calculated by pCLAMP software (Axon Instruments). Experiments were conducted with a HEKA EPC-10 patch clamp amplifier (HEKA, Harvard Bioscience) with signals being low-pass filtered at 2 kHz before undergoing digitization at 4 kHz. Cell capacitance and access resistance were compensated prior to each strain test sweep. Data were stored for off-line analysis.

Experimental protocol. For experiments, supplemented medium M199 was replaced by pH-buffered HBSS (pH 7.40) and the FCCD was firmly mounted to the SS by means of two clamps (*cf. Figure 1 of the article*). Thereafter, a filled patch pipette was mounted on the SICM head and positioned above the middle of the strain area of the FCCD. The pipette was lowered until the FCCD membrane surface was detected by the SICM. Thereafter the z-calibration was executed and the data stored for feed-forward z-compensation during all experiments with a given FCCD. Following selection of a cell to be investigated, a picture was acquired using the HRCam and the SSL vs. SSR balancing was adjusted such that the point of subsequent seal formation showed minimal displacement in response to a sinusoidal test strain. Next, the patch pipette was lowered and positioned above the point of intended seal formation followed by establishment of whole-cell recording configuration using standard procedures. After compensation of cell capacitance and access resistance, the membrane potential of the cell was determined using current clamp zero before starting the predefined strain protocols that were conducted in voltage clamp mode. Individual experiments were concluded either after successful completion of the protocols or if the gigaseal integrity became compromised. Thereafter, a new cell was chosen and, after rebalancing of SSL vs. SSR, a new experiment was started. All experiments were performed at room temperature.

Fluorescence based strain-to-cell transmission assessment. To investigate the fidelity by which cells followed mechanical deformation of the substrates, NIH3T3 cells grown in FCCDs were labeled using 1 μL of CellMask diluted in 1 ml of HBSS (green plasma membrane stain; ThermoFisher, C37608). After a 10 min incubation, the preparations were washed 3 times with HBSS. The fluorophore was excited with light from a 470 nm LED source (Thorlabs, M470L4-C4) that passed through an excitation filter (458/64 nm; Semrock) before being deflected towards the objective (Zeiss, 40 x; NA 0.65; Ph2) by a dichroic mirror (FF510-Di01-25x36, Semrock). Emitted fluorescence was bandpass filtered (535 ± 50 nm; Semrock) and images acquired with a CMOS camera (Ximea, MQ042MG-CM).

Data analysis. Data were analyzed with Matlab (Mathworks, Matlab 2019a). Data are presented either as raw data or as mean ± SD.